Tropical waves and the quasi-biennial oscillation in a 7-km global climate simulation

Laura A. Holt* and M. Joan Alexander

NorthWest Research Associates, Boulder, Colorado

Lawrence Coy

Global Modeling and Assimilation Office, NASA Goddard Space Flight Center, Greenbelt, Maryland, and Science Systems and Applications Inc, Lanham, Maryland

Andrea Molod

Earth System Science Interdisciplinary Center, University of Maryland, College Park, Maryland

William Putman and Steven Pawson

Global Modeling and Assimilation Office, NASA Goddard Space Flight Center, Greenbelt, Maryland

Corresponding author address: Laura A. Holt, NorthWest Research Associates, 3380 Mitchell Lane, Boulder, CO 80301.

E-mail: laura@nwra.com

ABSTRACT

We have investigated tropical waves and their role in driving a quasi-biennial oscillation (QBO)-like signal in stratospheric winds in a global 7-km horizontal resolution atmospheric general circulation model. The Nature Run (NR) is a two-year global mesoscale simulation of the Goddard Earth Observing System (GEOS-5) model. In the tropics, there is evidence that the NR supports a broad range of convectively generated waves. The NR precipitation spectrum resembles the observed spectrum in many aspects, including the preference for westward propagating waves. However, even with very high horizontal resolution and a healthy population of resolved waves, the zonal force provided by the resolved waves is still too low in the QBO region and parameterized gravity wave drag is the main driver of the NR QBO-like oscillation (NR-QBO). We suggest that causes include coarse vertical resolution and excessive dissipation. Nevertheless, the very high resolution NR provides an opportunity to analyze the resolved wave forcing of the NR-QBO. In agreement with previous studies, we find that large-scale Kelvin and small-scale waves contribute to the NR-QBO driving in eastward shear zones and small-scale waves dominate the NR-QBO driving in westward shear zones. Waves with zonal wavelength $<$1000 km account for up to half of the small-scale ($<$3300 km) resolved wave forcing in eastward shear zones and up to 70% of the small-scale resolved wave forcing in westward shear zones of the NR-QBO.

1. Introduction

Equatorial lower stratospheric zonal mean winds display a quasi-biennial oscillation (QBO) that is characterized by alternating eastward and westward winds descending through the stratosphere. The average period of the QBO, which has been continuously observed since 1953, is approximately 28 months, with a range of 22–34 months (Baldwin et al. 2001). The QBO is a wave-mean flow interaction phenomenon, driven by tropical Kelvin, mixed Rossby-gravity, inertia-gravity, and small-scale gravity waves (Lindzen and Holton 1968; Holton and Lindzen 1972; Dunkerton 1997). It is highly predictable at timescales of a year or more (Scaife et al. 2014).

Model experiments suggest that the frequency and amplitude of the QBO may change with changing climate (Kawatani and Hamilton 2013), however the sign and magnitude of predicted future changes are sensitive to highly uncertain model details (Schirber et al. 2014a). Furthermore, the QBO is known to modulate tropical-extratropical teleconnections (Scaife et al. 2014) and tropical cyclone activity (e.g., Camargo and Sobel 2010), and improved simulation of the QBO has been shown to improve skill in seasonal to interannual climate predictions (e.g. Thompson et al. 2002; Boer and Hamilton 2008; Scaife et al. 2014). Despite this, most models participating in the recent Climate Model Intercomparison Project (CMIP5) (Taylor et al. 2012) do not simulate the QBO. Successful simulation of the QBO in global models requires combined momentum forcing from large-scale equatorial waves and small-scale gravity waves. Climate models that simulate a realistic QBO usually rely on a parameterization for the gravity wave momentum forcing because of resolution limitations (Scaife et al. 2000; Giorgetta et al. 2002; Richter et al. 2014; Schirber et al. 2014b). Simulating a realistic QBO is challenging because it is extremely sensitive to many model parameters, such as horizontal and vertical resolution, gravity wave parameterization and

dynamical core (Anstey et al. 2015; Giorgetta et al. 2002; Kodama et al. 2015; Kawatani et al. 2010; Schirber et al. 2014b; Yao and Jablonowski 2015).

Several climate model experiments have simulated a QBO-like tropical wind oscillation without parameterized gravity waves with various degrees of realism (Takahashi 1996; Horinouchi and Yoden 1998; Hamilton et al. 1999; Watanabe et al. 2008; Kawatani et al. 2010). These and other studies have identified several necessary ingredients for realistic simulation of the QBO: (i) high-frequency variability in precipitation and latent heating to ensure sufficient wave generation, (ii) high vertical resolution (at least 700 m) to properly represent the wave-mean flow interaction in QBO shear zones, and (iii) sufficient gravity wave momentum flux, either parameterized or resolved. From their simulations without parameterized gravity waves, Horinouchi and Yoden (1998) noted the need for unusually weak model horizontal diffusion as necessary for simulation of the QBO in coarse horizontal resolution models, but hypothesized that this condition would not be necessary in higher horizontal resolution models. Kawatani et al. (2010) analyzed the wave forcing responsible for driving the QBO in a model with 60-km horizontal resolution and 300 m vertical resolution and moderate diffusion, and found that more than half of the forcing driving the QBO was due to internal inertial gravity waves with wavelengths less than $\sim$3300 km.

This study examines equatorial stratospheric winds, waves, and precipitation in a free-running global climate model with horizontal resolution near 7 km, nearly an order of magnitude finer than the model used in the Kawatani et al. (2010) study. The goal of this study is to investigate the dependence of tropical wave driving on the scale of the resolved waves and the relationship between resolved and parameterized wave driving in a mesoscale global model. The model has limited vertical resolution, but has a very realistic representation of tropical precipitation and small-scale waves, providing a unique representation of tropical dynamics and associated gravity wave forcing for study.

The paper is organized as follows. We describe the model in Section 2. We describe features of the model QBO-like oscillation and compare them to reanalyses in Section 3. Since the resolved waves that contribute to driving the QBO are generated by tropical precipitation variability, we evaluate tropical precipitation variability with respect to observations in Section 4. We analyze the resolved waves and their role in the zonal momentum budget in Section 5. In Section 6 we compare the model resolved wave forcing to the parameterized wave forcing as well as the total force derived from reanalyses. In Section 7 we show the effects of resolution on resolved wave forcing. Finally, we provide a summary of our results and concluding remarks in Section 8.

2. GEOS-5 Nature Run

The Nature Run (NR) (Gelaro et al. 2015; Putman et al. 2014) is a two-year 7-km horizontal resolution non-hydrostatic global mesoscale simulation produced with the Goddard Earth Observing System (GEOS-5) atmospheric general circulation model. The simulation was performed with finite-volume (FV) dynamics (based on Lin (2004)) on a cubed-sphere horizontal grid (Putman and Lin 2007) with explicit diffusion from second-order divergence damping. The second-order divergence damping coefficient was $0.2 \times \Delta A_{min}/\Delta t$, where ΔA_{min} is the smallest grid cell area in the domain. This provided a strong damping on the divergent component of the flow. The external mode damping was $0.02 \times \Delta A_{min}/\Delta t$. The physics, vertical remapping, and dynamics time steps were 300, 75, and 5 s, respectively. The NR has 72 vertical levels from the surface up to $\sim$0.01 hPa ($\sim$85 km). The vertical resolution ranges from $\sim$1 km near the tropopause to $\sim$2 km near the stratopause, which, as mentioned in the introduction, has been shown by previous studies to be insufficient for a realistic simulation of the QBO. The model was forced with prescribed sea-surface temperatures and sea-ice, and surface emissions/uptake of aerosols and trace gases, all based on measurements from May 2005–June 2007.

Convection in GEOS-5 is parameterized using the Relaxed Arakawa-Schubert scheme of Moorthi and Suarez (1992). Prognostic cloud cover and cloud water and ice is calculated using the scheme of Bacmeister et al. (2006), with profiles of total water probability distribution function calculated as in Molod (2012). The orographic gravity wave parameterization is McFarlane (1987) and the non-orographic gravity wave parameterization is based on Garcia and Boville (1994). The phase speed spectrum is launched from 400 hPa with a range of ± 40 m s^{-1} in increments of 10 m s^{-1}. The orographically generated waves depend on the sub-grid scale topographic variance, which is a function of the model resolution. As the model resolution increases, the variance is adjusted to account for the increase in resolved topography and explicitly resolved gravity waves. Non-orographic gravity waves are specified with an equatorial peak in momentum flux (see Figure 3 in Molod et al. (2015)), and the period of the QBO is sensitive to the details of this specification similar to previous reports (Giorgetta et al. 2006; Schirber et al. 2014b).

For the analysis of the NR, we used output that was interpolated to $0.5^\circ \times 0.5^\circ$ (lon $\times$ lat) horizontal resolution and on the model vertical grid, except when the NR is directly compared to reanalysis. When comparing to reanalysis we used the NR pressure level data, which was output on the same pressure levels as the reanalysis.

3. Comparison of NR-QBO to MERRA-2 QBO

This section compares the tropical winds found in the NR with those in MERRA (Modern-Era Retrospective Analysis for Research and Applications), version 2 (MERRA-2). A description of the MERRA reanalysis system is found in Rienecker et al. (2011). The new ongoing MERRA-2 reanalysis (1980-present, Bosilovich et al. 2015) improves on MERRA by assimilating observations from current instruments (such as hyperspectral radiances, global positioning system bending angles, and limb sounding temperature and ozone profiles) that the original MERRA system was

unable to incorporate into the analysis system, and thus is a natural follow-on to MERRA. An especially important change from MERRA to MERRA-2 was an increase in the model's parameterized gravity wave drag (GWD) that allows for a model internally-generated QBO, a feature not found in the original MERRA general circulation model (GCM) (Molod et al. 2015). This change helped reduce the MERRA-2 data assimilation system's dependence on observations to capture the QBO dynamics. We note that the gravity wave parameterization and divergence damping schemes are identical in the NR and MERRA-2. Pressure level data on 42 constant pressure levels from the surface up to 0.1 hPa with a horizontal resolution of 0.635° by 0.5° longitude by latitude was used for the data analysis.

Figure 1 shows the monthly-averaged zonal mean zonal wind for (a) the NR compared to (b) MERRA-2 (Global Modeling and Assimilation Office (GMAO) 2015a). Although the NR is a free-running atmospheric model, it was initialized with MERRA winds. The NR has a QBO-like signal (NR-QBO) with similar timing as MERRA-2. The NR-QBO completes one cycle in the 24-month integration, which is slightly shorter than the time that MERRA-2 takes to complete the cycle. With only one simulated cycle in the NR, we avoid placing too much significance on this shorter period. The winds in the NR are stronger than in MERRA-2 during the eastward phase, especially in the upper half of the plot range. As in MERRA-2, the NR winds are larger in magnitude during the westward phase than in the eastward phase, however the difference is not quite as pronounced in the NR as it is in MERRA-2. This can be seen more clearly in Figs. 1c and d, which show the average zonal mean zonal wind for eastward (red) and westward (blue) winds, i.e., the red line is calculated at each pressure level as the average over all times for which the zonal mean zonal wind is positive. The lines from panel c are replotted in panel d as dashed lines for ease of comparison. Overall, there is fairly good agreement between the NR and MERRA-2 average zonal mean zonal winds. The largest differences between the NR and MERRA-2 average

zonal mean zonal wind are in the westward winds between 50 and 30 hPa and the eastward winds above $\sim$30 hPa.

4. Evaluation of NR tropical precipitation

Precipitation variability is a key indicator of tropical wave generation. The dominant source of vertically propagating waves that drive the QBO is latent heat release in precipitating clouds (Holton 1972; Ricciardulli and Garcia 2000; Stephan and Alexander 2015). Figure 2 compares the zonal wavenumber-frequency spectrum of tropical precipitation (15°S–15°N) of the NR and the Tropical Rainfall Measuring Mission (TRMM) satellite (3B42 product, Huffman et al. 2007). To produce the spectra we followed the method of Kim and Alexander (2013), which compared TRMM to several reanalyses including MERRA. Briefly, 3-hourly averages of precipitation from the NR were binned to $1.875° \times 1.875°$, and a fast Fourier transform was performed on 36-day time periods with a 6-day overlap and taper. Figure 2a is the average over the 2 years of the NR, and Figure 2b is the 3-year average of TRMM from January 2005 through December 2007. Compared to TRMM, the NR has lower spectral densities at higher frequencies; however, the NR represents the higher frequency variability better than the reanalyses included in Kim and Alexander (2013). The NR also reproduces the preference for westward propagating waves seen in TRMM. Overall, the NR is able to realistically represent a broad range of tropical precipitation variability and convectively coupled waves, which are the sources of vertically propagating waves that drive the QBO. The mean tropical precipitation rate is 0.23 mm hr^{-1} in the NR compared to 0.16 mm hr^{-1} in TRMM. The NR tropical precipitation rate is at the high end of those found in reanalysis data sets (0.19–0.23 mm hr^{-1}) (Kim and Alexander 2013).

Dividing the antisymmetric and symmetric components of Figures 2(a) and 2(b) by the smoothed background spectra, as described in Wheeler and Kiladis (1999), reveals the preferred modes of the

sub-monthly precipitation variability. Figures 2(c) and 2(d) show the antisymmetric component of the precipitation variance in the NR and TRMM, respectively, and Figures 2(e) and 2(f) show the symmetric components. Theoretical dispersion curves for even and odd meridional mode number equatorial waves for equivalent depths of 12, 25, and 50 m are also plotted, assuming a zero wind basic state. Equatorial wave modes include Kelvin, equatorial Rossby, mixed Rossby-gravity, and eastward and westward inertia-gravity waves. It can be seen in Figures 2(c–f) that the NR preferred modes of variability closely match the preferred modes of variability in TRMM. Although the spectrum of temperature is not shown here, we note that typical Kelvin wave and mixed Rossby-gravity wave amplitudes in temperature at $\sim$100 hPa are $\pm$2.5 K and $\pm$1.3 K, resepectively, which are comparable to observational estimates (e.g., Alexander et al. 2008; Alexander and Ortland 2010).

The spectrum in Figure 2a indicates the organization of precipitation variability, but in an average sense. Occurrences of precipitation extremes are another separate indicator of the strength of high frequency wave generation. Gelaro et al. (2015) (Figure 3.29) showed that the probability distribution of NR precipitation is higher than TRMM at both low ($<$ 1 mm hr^{-1}) and high ($>$ 20 mm hr^{-1}) precipitation rates and lower than that of TRMM at intermediate precipitation rates. The infrequent high precipitation rates correspond to intermittent, localized bursts of precipitation and are strong sources of gravity waves, whereas the frequent low precipitation rates correspond to more or less continuous drizzle.

5. Resolved waves and wave driving of the NR-QBO

The zonal force generated by the NR resolved waves can be studied using wave-mean flow theory. The transformed Eulerian-mean (TEM) (Andrews and McIntyre 1976) zonal mean zonal

momentum equation in log-pressure coordinates is:

$$\frac{\partial \overline{u}}{\partial t} - \overline{v}^* \left[f - \frac{1}{a\cos\phi}\frac{\partial}{\partial \phi}\left(\overline{u}\cos\phi\right)\right] + \overline{w}^* \frac{\partial \overline{u}}{\partial z} = \frac{1}{\rho_0 a\cos\phi}\nabla\cdot\mathbf{F} + \overline{X} \tag{1}$$

where $\rho_0 = \rho_s \exp\left(-z/H\right)$, ρ_s is a reference density, H is a constant scale-height, $z = -H\ln p/p_s$, p is pressure, p_s is a reference pressure, u, v, w are zonal, meridional, and vertical velocity, f is the Coriolis parameter, a is Earth's radius, ϕ is latitude, $\mathbf{F}$ is the Eliassen-Palm (EP)-flux vector, and X includes all other dissipative forces. We chose p_s =1000 hPa, H =7 km, and ρ_s =1.225 kg m^{-3}. Overbars denote zonal means and * denotes residual circulation variables. The divergence of the EP-flux, which represents the wave forcing in the TEM zonal momentum equation, is

$$\nabla\cdot\mathbf{F} = \left[\frac{1}{a\cos\phi}\frac{\partial}{\partial\phi}\left(F_\phi\cos\phi\right) + \frac{\partial F_z}{\partial z}\right] \tag{2}$$

and the horizontal and vertical components of the EP-flux vector are

$$F_\phi = \rho_0 a\cos\phi\left(\frac{\overline{v'\theta'}}{\partial\overline{\theta}/\partial z}\frac{\partial\overline{u}}{\partial z} - \overline{u'v'}\right) \tag{3}$$

and

$$F_z = \rho_0 a\cos\phi\left\{\frac{\overline{v'\theta'}}{\partial\overline{\theta}/\partial z}\left[f - \frac{1}{a\cos\phi}\frac{\partial}{\partial\phi}\left(\overline{u}\cos\phi\right)\right] - \overline{u'w'}\right\} \tag{4}$$

where θ is potential temperature and the primed quantities are deviations from the zonal mean.

The components of the EP-flux vector can also be computed as a function of zonal wavenumber, k, and frequency, ω:

$$F_\phi(k,\omega) = \rho_0 a\cos\phi\left\{\frac{\Re[V(k,\omega)\widetilde{\Theta}(k,\omega)]}{\partial\overline{\theta}/\partial z}\frac{\partial\overline{u}}{\partial z} - \Re[U(k,\omega)\widetilde{V}(k,\omega)]\right\} \tag{5}$$

$$F_z(k,\omega) = \rho_0 a\cos\phi\left\{\frac{\Re[V(k,\omega)\widetilde{\Theta}(k,\omega)]}{\partial\overline{\theta}/\partial z}\left[f - \frac{1}{a\cos\phi}\frac{\partial}{\partial\phi}\left(\overline{u}\cos\phi\right)\right] - \Re[U(k,\omega)\widetilde{W}(k,\omega)]\right\} \tag{6}$$

where $\Re$ denotes the real part and the tilde denotes the complex conjugate. $U(k,\omega)$, $V(k,\omega)$, $W(k,\omega)$, and $\Theta(k,\omega)$ are the two-dimensional Fourier transforms of $u(\lambda,t)$, $v(\lambda,t)$, $w(\lambda,t)$, and $\theta(\lambda,t)$, where λ is longitude and t is time. In the following analysis we used hourly instantaneous, $0.5^\circ \times 0.5^\circ$ (lon $\times$ lat) variables to compute the spectra. We note that hourly average covariances of w and u were also saved, but we found that the $w'u'$ component of the vertical EP-flux divergence was almost identical to that obtained with the hourly instantaneous files for the majority of the simulation.

Figure 3 shows the wavenumber-frequency spectrum of the vertical component of the EP-flux vector (Eq. 6), F_z, averaged over the 2-year NR between 10°S and 10°N and over the pressure range ~118–100 hPa. We chose the common tropical convention, where eastward propagating waves are displayed with positive flux and westward waves with negative flux. Note that some positive flux appears for negative zonal wave numbers since the phase speeds here are relative to the ground and not the background wind. The EP-flux spectrum shows that the NR has a strong population of atmospheric waves across the full range of frequencies with the largest power concentrated at the lower frequencies (i.e., a red spectrum). The NR EP-flux spectrum also has a realistic distribution of phase speeds. In particular, the double lobe structure centered around ± 20 and ± 50 m s^{-1} is similar to Figure 11a from Ricciardulli and Garcia (2000), which shows vertical EP-flux derived from the global cloud imagery (GCI) dataset.

The wavenumber-frequency spectrum of the EP-flux divergence term in Eq. 1 can be obtained by plugging $F_\phi(k,\omega)$ and $F_z(k,\omega)$ into Eq. 2 and dividing by $\rho_0 a \cos\phi$. Henceforth, EP-flux divergence will be used to refer to the first term on the right hand side of Eq. 1. Figure 4 shows wavenumber-frequency spectra of EP-flux divergence for regions with a strong eastward shear with height (Fig. 4a) and a strong westward shear with height (Fig. 4b). The region of strong

eastward shear is August 2005 between 20 and 10 hPa, and the region of strong westward shear is July 2006 between 20 and 10 hPa (see Fig. 1a). Note that there is significant EP-flux divergence for the highest phase speed gravity waves at these levels.

Figure 5 shows the total resolved EP-flux divergence as a function of pressure and time (a) and the contribution from (b) westward propagating small-scale waves, (c) westward propagating large-scale, low-frequency waves, (d) eastward propagating small-scale waves, and (e) eastward propagating large-scale, low-frequency waves to the total. The large-scale, low-frequency contribution was obtained by summing the monthly EP-flux divergence at each level over $1 \leq |k| \leq 11$ and $\omega < 1$ cpd. The large-scale, low-frequency waves include the equatorial wave modes, such as Kelvin, equatorial Rossby, mixed Rossby-gravity, and eastward and westward inertia-gravity waves. The small-scale contribution was obtained by summing over $|k| \geq 12$ ($\sim$3300 km). The eastward and westward components were obtained by summing only positive or negative values of EP-flux divergence for each region.

The resolved EP-flux divergence in the westward shear zones of the NR-QBO is dominated by small-scale westward propagating waves between $\sim$50 and 10 hPa (Figure 5b), which contribute $\sim$60% of the total westward resolved wave forcing (averaged over the westward shear zones). Large-scale, low-frequency westward propagating waves contribute 30-40% of the total westward resolved wave forcing above 30 hPa. The large increase in negative EP-flux divergence from December 2005 through February 2006 in Figure 5c is likely due to large-scale planetary and synoptic waves from the NH winter that propagate into the tropics during the eastward phase of the NR-QBO and may contribute to the slower descent of the westerly wind in that period. Averaged over the eastward shear zones, the small-scale eastward propagating waves contribute $\sim$35% of the total eastward resolved wave forcing (Figure 5d), and eastward propagating large-scale, low-frequency waves make up half of the eastward resolved wave forcing (Figure 5e). The

rest of the EP-flux divergence is provided by regions of the spectrum not included in Figures 5b-e. For example, large-scale, high frequency waves contribute less than 10% of the EP-flux divergence in both eastward and westward shear zones.

Figure 6 shows the distribution of small-scale EP-flux divergence in different wavenumber bins at (a) ∼15 hPa, (b) ∼30 hPa, and (c) ∼50 hPa. Gravity waves with wavelength of ∼1000 km or less ($k \geq 40$) contribute substantially to the small-scale EP-flux divergence at all levels. In eastward shear zones they account for up to half of the small-scale forcing, and in westward shear zones they account for $\sim 55-70\%$ of the small-scale forcing. The smallest-scale resolved waves ($k \geq 200$; $\lambda_x \lesssim 200$ km) contribute about 3% of the small-scale forcing in eastward shear zones and up to 7% of the small-scale forcing in westward shear zones at ∼15 hPa. However, these estimates of the smallest-scale resolved wave contributions should be considered with caution due to the unrealistically large dissipation at the smallest model scales as discussed below.

These results are in reasonable agreement with Kawatani et al. (2010) with respect to the proportion of resolved wave forcing coming from large- and small-scale waves, but the magnitude of the total resolved wave forcing is lower in the NR. The ever-present areas of light blue and red in Figure 5(b-e) highlight one potential reason why the total resolved wave forcing is relatively low in the NR. If waves dissipated only as they approached their critical levels where their vertical scales shrink to small values, dissipation would be limited to eastward waves in eastward shear and westward waves in westward shear. However, it is clear that both eastward and westward propagating waves are damped simultaneously throughout the entire simulation. Hence it appears as if dissipation is acting everywhere on the waves in the model without sufficient selectivity for vertical scale. Further evidence of this is seen in the kinetic energy power spectrum (shown in Figure 2.10 in Gelaro et al. (2015)). For long horizontal wavelengths >1000 km, the slope of the power spectrum closely follows the established n^{-3} law, where n is total horizontal wavenumber.

At shorter scales in the observations, the spectrum transitions to $n^{-5/3}$ characteristic of observed gravity waves (e.g. Nastrom and Gage 1985), but in the NR, the slope of the spectrum never reaches $n^{-5/3}$. Instead, the NR spectrum sharply falls off as the horizontal wavelengths approach the smaller resolved scales. This is characteristic of unrealistically large dissipation at the smaller resolved scales in the model.

Figure 7 examines the potential effects of this unrealistically large dissipation by addressing the question: how much cancelation due to simultaneous eastward and westward forcing occurs in the NR? The solid lines represent the net EP-flux divergence in the NR, whereas the dashed lines show what the EP-flux divergence would be if the wave dissipation was limited to eastward waves in eastward shear zones and westward waves in westward shear zones. The EP-flux divergence is reduced by about half in the westward shear zones and reduced by 84–95% between 50 and 10 hPa in the eastward shear zones. The unrealistically large damping is most likely due to the degree of explicit divergence damping and implicit dissipation associated with the numerical scheme. For example, Yao and Jablonowski (2015) showed that different dynamical core options in NCAR's Community Atmosphere Model, version 5 (CAM5) impacted the ability of the model to sustain QBO-like oscillations in a simple dry GCM setup with the Held and Suarez (1994) forcing scheme. In particular, a simulation with the gridpoint-based FV dynamical core did not sustain the initialized QBO, while simulations with the Eulerian, spectral element and semi-Lagrangian cores developed spontaneous QBO-like oscillations. All model simulations were run with identical vertical grids ($\Delta z = 1.25$ in the stratosphere) and horizontal resolutions of $\sim 2^\circ \times 2^\circ$. The wave activity and EP-flux divergence were reduced in the FV dynamical core simulation, which the authors pointed out could be attributable to the FV dynamical core being more diffusive than the other dynamical cores. Since not all simultaneous wave dissipation can be attributed to the un-

realistically large damping in the model, the numbers given above for the NR should be regarded as an upper limit of how the dissipation is opposing the NR-QBO forcing.

In addition to small-scale dissipation, there appears to be some cancellation due to large-scale waves. The large-scale westward propagating waves (Figure 5c) have the strongest cancelation (i.e., negative EP-flux divergence is large in eastward shear zones, for example in June-August 2005 above 20 hPa). This most likely is a result of planetary waves from the winter hemisphere that penetrate into the tropics when the QBO is transitioning from easterly to westerly. With only two years of simulation, it is not possible to know if this would be a common or rare occurrence in the model.

6. Comparison to MERRA-2 zonal force

To obtain a realistic model QBO, we expect that the sum of the resolved EP-flux divergence and the parameterized GWD, if present, be comparable to the total zonal force obtained from observations. To evaluate whether this is true for the NR, we have chosen to use MERRA-2 since it has a QBO that closely matches observations. Figure 8 shows the sum of the EP-flux divergence from resolved waves and the GWD from parameterized waves in the NR as well as the total zonal force in MERRA-2. The total zonal force refers to the lefthand side of Equation 1, and the resolved EP-flux divergence and parameterized GWD are included on the righthand side of Equation 1. We computed the residual circulation needed to estimate the total zonal force for MERRA-2 by iteratively solving the thermodynamic equation (Solomon et al. 1986). To summarize the method, radiative heating rates from MERRA-2 (Global Modeling and Assimilation Office (GMAO) 2015b) were used to obtain an initial approximation of $\overline{w}^*$, which was then used to obtain the TEM streamfunction, $\overline{\Psi}^*$. From $\overline{\Psi}^*$ we evaluated $\overline{v}^*$, which was in turn used to correct the initial approximation of $\overline{w}^*$ and the process was iterated until the solution converged to

less than 1% difference from one iteration to the next. Figure 9 shows $\overline{w}^*$ for MERRA-2 (blue) as well as the NR (red). For comparison, the dashed red line shows $\overline{w}^*$ for the NR using the kinematic method of calculation described in Coy and Swinbank (1997). This method uses the meridional wind and temperature to calculate $\overline{v}^*$ from the definition given in Andrews and McIntyre (1976) and the TEM mass continuity equation to obtain $\overline{w}^*$. Figure 9 shows that the two methods for calculating $\overline{w}^*$ agree extremely well. We used the pressure-level variables to calculate the NR residual circulation for a direct comparison to MERRA-2. The overall shape and magnitude of $\overline{w}^*$ are very similar for the NR and MERRA-2.

With the iterative thermodynamic method, values of MERRA-2 $\overline{w}^*$ are $\sim$ 0.3, 0.2, and 0.4 mm s^{-1} at 18, 21, and 27 km respectively. Using observed water vapor to estimate $\overline{w}^*$, Schoeberl et al. (2008) obtained values of $\sim$ 0.4, 0.3, and 0.6 mm s^{-1} at 18, 21, and 27 km respectively. MERRA-2 $\overline{w}^*$ values are also comparable to MERRA and other reanalysis and model estimates (Abalos et al. 2015; Seviour et al. 2012; Osprey et al. 2013).

As stated above, to obtain a realistic model QBO the sum of the resolved EP-flux divergence and the parameterized GWD should be comparable to the total zonal force in MERRA-2. Indeed they are similar, however there are some significant differences especially towards the upper and lower levels shown in Figure 8. For example, in the NR the sum of the resolved EP-flux divergence and parameterized GWD is larger than the total zonal force in MERRA-2, especially at the upper levels in the westward phase of the QBO. This could explain why the NR-QBO completes its cycle at a somewhat faster rate than in MERRA-2, even though they started with the same winds.

Between 40 and 10 hPa, the resolved EP-flux divergence is between $\sim$8 and 40 times smaller than the parameterized GWD averaged over regions of eastward shear and only $\sim$3–4 times smaller averaged over regions of westward shear. The parameterized GWD is comparable in magnitude to the total zonal force from MERRA-2 at most levels. Perhaps most importantly, the large

parameterized gravity wave forcing appears to be necessary to counter the effects of non-selective wave dissipation, which is evidenced by the similarity of the dashed profiles in Figure 7 to the MERRA-2 total force in Figure 8. In other words, if the resolved waves instead selectively dissipated in the shear zones where their vertical scales grew short the parameterized gravity waves could be greatly reduced or eliminated.

7. EP-flux divergence and model resolution

To better understand the effects of horizontal and vertical resolution on resolved EP-flux divergence, Figure 10 compares EP-flux divergence profiles for three model runs: (blue) a control run with 1° horizontal resolution and 72 vertical levels, (orange) a run with 1° horizontal resolution and 137 vertical levels, and (red) the NR (0.0625° horizontal resolution and 72 vertical levels). The profiles are averaged over the descending westward phase of the QBO so that the zonal mean zonal wind profiles are similar with zero-wind lines near the same level. Note that we used pressure-level data (interpolated from the different model levels to a common set of pressure levels) to calculate the EP-flux divergence for each model run.

Doubling the vertical resolution increases the EP-flux divergence by about a factor of 2 near the zero-wind line, whereas increasing the horizontal resolution (by a factor of 16, or 256 additional points within each grid cell) increases the EP-flux divergence by almost a factor of 4 near the zero-wind line ($\sim$20 hPa). However, the parameterized GWD from the NR is almost a factor of 4 larger still than the resolved EP-flux divergence in the NR between 20 and 10 hPa. It is uncertain if doubling the vertical resolution in the NR would double the EP-flux divergence. The combined effect of increasing both horizontal and vertical resolution could be more than additive as higher vertical resolution would support more of the wave spectrum generated by higher horizontal resolution and reduce dissipation. While it is possible that doubling the vertical resolution alone could

permit a NR-type simulation to produce a QBO without parameterized gravity wave drag, reduced divergence damping might still also be necessary.

8. Summary and conclusions

We have investigated tropical waves and their role in driving the QBO-like oscillation in the global 7-km horizontal resolution NR. We found that the NR has a realistic representation of a broad range of convectively generated waves. The NR precipitation spectrum resembles the TRMM spectrum in many ways, including the preference for westward propagating waves. The NR-QBO completes one cycle in the $\sim$24 month simulation, which falls within the range of observed QBO periods. The NR-QBO cycle is slightly shorter than MERRA-2 for the same time period even though the NR was initialized with MERRA winds. Overall, the average zonal mean zonal winds agree fairly well between the NR and MERRA-2. Both NR and MERRA-2 winds are larger in magnitude during the westward phase than in the eastward phase. The largest discrepancies are that the winds in the NR are stronger than in MERRA-2 during the eastward phase above $\sim$30 hPa, and the winds in the NR are weaker than in MERRA-2 during the westward phase between $\sim$50 and 30 hPa.

We analyzed the resolved wave spectrum and contribution of different scales of waves to the EP-flux divergence and found that in eastward shear zones the resolved forcing is roughly split between large-scale Kelvin and small-scale ($k \geq 12$) waves. In westward shear zones, the resolved forcing is dominated by small-scale waves. We also found that gravity waves with zonal wavelength $\leq$1000 km are important drivers of the resolved EP-flux divergence and account for up to half of the small-scale resolved wave forcing in eastward shear zones and up to 70% of the small-scale resolved wave forcing in westward shear zones. The smallest-scale resolved waves ($\lesssim$ 200 km) also make up a non-trivial portion of the small-scale resolved wave forcing (up to 7% in

westward shear zones and 3% in eastward shear zones) despite unrealistically large dissipation at the smallest model scales.

Even with very high horizontal resolution and a reasonably realistic population of resolved waves, parameterized gravity wave drag is still the main driver of the NR-QBO. We showed evidence that increasing the vertical resolution would reduce the need to rely on parameterized GWD to obtain a QBO. We also hypothesized that increasing scale-selectivity in the diffusion scheme could reduce the need to rely on parameterized GWD. The experiments contrasting low and high horizontal and vertical resolutions showed that better resolution in either the horizontal or vertical increases the EP-flux divergence as expected, and increasing the vertical resolution had a much larger relative effect: doubling the vertical resolution doubled the EP-flux divergence, whereas a factor of 16 increase in horizontal resolution only quadrupled the EP-flux divergence.

Acknowledgments. We thank Dr. Ji-Eun Kim for providing the TRMM spectrum for Figure 2, and we thank 3 anonymous reviewers for their thoughtful and helpful suggestions. This work is funded by the NASA Global Modeling and Assimilation Office, Grant #NNX14O76G. This work was also supported by NASA's Modeling, Analysis and Prediction (MAP) program.

References

Abalos, M., B. Legras, F. Ploeger, and W. J. Randel, 2015: Evaluating the advective Brewer-Dobson circulation in three reanalyses for the period 1979–2012. *J. Geophys. Res. Atmos.*, **120**, 7534–7554, doi:10.1002/2015JD023182.

Alexander, M. J., and D. Ortland, 2010: Equatorial waves in High Resolution Dynamics Limb Sounder (HIRDLS) data. *J. Atmos. Sci.*, **115**, D24111, doi:10.1029/2010JD014782.

Alexander, S. P., T. Tsuda, Y. Kawatani, and M. Takahashi, 2008: Global distribution of atmospheric waves in the equatorial upper troposphere and lower stratosphere: COSMIC observations of wave mean flow interactions. *J. Geophys. Res.*, **113**, D24115, doi:10.1029/2008JD010039.

Andrews, D. G., and M. E. McIntyre, 1976: Planetary waves in horizontal and vertical shear: The generalized Eliassen-Palm relation and the mean zonal acceleration. *J. Atmos. Sci.*, **33**, 2031–2048.

Anstey, J. A., J. F. Scinocca, and M. Keller, 2015: Simulating the QBO in at Atmospheric General Circulation Model: Sensitivity to Resolved and Parameterized Forcing. *J. Atmos. Sci.*, **73**, 1649–1665, doi:10.1175/JAS-D-15-0099.1.

Bacmeister, J. T., M. J. Suarez, and F. R. Robertson, 2006: Rain re-evaporation, boundary layer convection interactions, and Pacific rainfall patterns in an AGCM. *J. Atmos. Sci.*, **63**, 3383–3403.

Baldwin, M. P., and Coauthors, 2001: The quasi-biennial oscillation. *Rev. Geophys.*, **39**, 179–229.

Boer, G., and K. Hamilton, 2008: QBO influence on extratropical predictive skill. *Climate Dyn.*, **31**, 987–1000.

Bosilovich, M. G., and Coauthors, 2015: MERRA-2: Initial Evaluation of the Climate. *Technical Report Series on Global Modeling and Data Assimilation*, NASA, NASA/TM-2015-104606, Vol. 39.

Camargo, S. J., and A. H. Sobel, 2010: Revisiting the influence of the quasi-biennial oscillation on tropical cyclone activity. *J. Climate*, **23**, 5810–5825.

Coy, L., and R. Swinbank, 1997: Characteristics of stratospheric winds and temperatures produced by data assimilation. *J. Geophys. Res.*, **102**, 25,763–25,781, doi:10.1029/97JD02361.

Dunkerton, T. J., 1997: The role of gravity waves in the quasi-biennial oscillation. *J. Geophys. Res.*, **102 (D22)**, 26 053–26 076.

Garcia, R. R., and B. A. Boville, 1994: Downward control of the mean meridional circulation and temperature distribution of the polar winter stratosphere. *J. Atmos. Sci.*, **51**, 2238–2245.

Gelaro, R., and Coauthors, 2015: Evaluation of the 7-km geos-5 nature run. *Technical Report Series on Global Modeling and Data Assimilation*, R. D. Koster, Ed., NASA, NASA/TM-2014-104606, Vol. 36.

Giorgetta, M. A., E. Manzini, and E. Roeckner, 2002: Forcing of the quasi-biennial oscillation from a broad spectrum of atmospheric waves. *Geophys. Res. Lett.*, **29 (8)**, 1245–1248, doi:10.1029/2002GL014756.

Giorgetta, M. A., E. Manzini, E. Roeckner, M. Esch, and L. Bengtsson, 2006: Climatology and forcing of the quasi-biennial oscillation in the MAECHAM5 model. *J. Climate*, **19**, 3882–3901.

Global Modeling and Assimilation Office (GMAO), 2015a: instM_3d_asm_Np: MERRA-2 3D IAU State Zonal Wind, Monthly Averaged 3-hourly (p-coord, 0.625x0.5L42), version 5.12.4, Greenbelt, MD, USA: Goddard Space Flight Center Distributed Active Archive Center (GSFC DAAC). doi:10.5067/2E096JV59PK7.

Global Modeling and Assimilation Office (GMAO), 2015b: tavgM_3d_tdt_Np: MERRA-2 3D Radiative Heating Rates, Monthly Averaged 3-hourly (p-coord, 0.625x0.5L42), version 5.12.4, Greenbelt, MD, USA: Goddard Space Flight Center Distributed Active Archive Center (GSFC DAAC). doi:10.5067/VILT59HI2MOY.

Hamilton, K., R. J. Wilson, and R. Hemler, 1999: Middle atmosphere simulated with high vertical and horizontal resolution versions of a GCM: Improvements in the cold pole bias and generation of a QBO-like oscillation in the tropics. *J. Atmos. Sci.*, **56**, 3829–3846.

Held, I. M., and M. J. Suarez, 1994: A proposal for the intercomparison of the dynamical cores of atmospheric general circulation models. *Bull. Amer. Meteor. Soc.*, **75**, 1825–1830, doi:{10.1175/1520-0477(1994)075,1825:APFTIO.2.0.CO;2.}

Holton, J. R., 1972: Waves in the equatorial stratosphere generated by tropospheric heat sources. *J. Atmos. Sci.*, **29**, 368–375.

Holton, J. R., and R. S. Lindzen, 1972: An updated theory for the quasi-biennial oscillation. *J. Atmos. Sci.*, **29**, 1076–1080.

Horinouchi, T., and S. Yoden, 1998: Wave-mean flow interaction associated with a QBO-like oscillation simulated in a simplified GCM. *J. Atmos. Sci.*, **55**, 502–526.

Huffman, G. J., and Coauthors, 2007: The TRMM multisatellite precipitiation analysis (TMPA): Quasi-global, multiyear, combined-sensor precipitation estimates at fine scales. *J. Hydrometeor.*, **8**, 38–55, doi:10.1175/JHM560.1.

Kawatani, Y., and K. Hamilton, 2013: Weakened stratospheric quasibiennial oscillation driven by increased tropical mean upwelling. *Nature*, **497**, 478–481, doi:10.1038/nature12140.

Kawatani, Y., K. Sato, T. J. Dunkerton, S. Watanabe, S. Miyahara, and M. Takahashi, 2010: The roles of equatorial trapped waves and internal intertia-gravity waves in driving the quasi-biennial oscillation. Part I: Zonal mean wave forcing. *J. Atmos. Sci.*, **67**, 963–980, doi:10.1175/2009JAS3222.1.

Kim, J.-E., and M. J. Alexander, 2013: Tropical precipitation variability and convectively coupled equatorial waves on submonthly time scales in reanalysis and TRMM. *J. Climate*, **26**, 3013–3030, doi:10.1175/JCLI-D-12-00353.1.

Kodama, C., and Coauthors, 2015: A 20-year climatology of a NICAM AMIP-type simulation. *J. Meteor. Soc. Japan*, **93**, 393–424, doi:10.2151/jmsj.2015-024.

Lin, S.-J., 2004: A 'vertically Lagrangian' finite-volume dynamical core for global models. *Mon. Wea. Rev.*, **132**, 2293–2307.

Lindzen, R. S., and J. R. Holton, 1968: A theory of the quasi-biennial oscillation. *J. Atmos. Sci.*, **25**, 1095–1107.

McFarlane, N. A., 1987: The effect of orographically excited gravity wave drag on the general circulation of the lower stratosphere and troposphere. *J. Atmos. Sci.*, **44 (14)**, 1775–1800.

Molod, A., 2012: Constraints on the profiles of total water PDF in AGCMs from AIRS and a high-resolution model. *J. Climate*, **25**, 8341–8352.

Molod, A., L. Takacs, M. Suarez, and J. Bacmeister, 2015: Development of the GEOS-5 atmospheric general circulation model: evolution from MERRA to MERRA2. *Geosci. Model Dev.*, **8**, 1339–1356, doi:10.5194/gmd-8-1339-2015.

Moorthi, S., and M. J. Suarez, 1992: A parameterization of moist convection for general circulation models. *Mon. Wea. Rev.*, **120**, 3877–3886, doi:10.1029/1998JD200092.

Nastrom, G. D., and K. S. Gage, 1985: A climatology of atmospheric wavenumber spectra of wind and temperature observed by commercial aircraft. *J. Atmos. Sci.*, **42**, 950–960, doi:10.1175/1520-0469(1985)042⟨0950:ACOAWS⟩2.0.CO;2.

Osprey, S. M., L. J. Gray, S. C. Hardiman, N. Butchart, and T. J. Hinton, 2013: Stratospheric variability in twentieth-century CMIP5 simulations of the Met Office Climate Model: High top versus low top. *J. Climate*, **26**, 1595–1606, doi:10.1175/JCLI-D-12-00147.1.

Putman, W. M., A. M. da Silva, L. Ott, and A. Darmenov, 2014: Model configuration for the 7-km GEOS-5.12 Nature Run, Ganymed Release (Non-hydrostatic 7 km Global Mesoscale Simulation). *GMAO Office Note No. 5.0 (Version 1.0)*, NASA, 18 pp, available from http://gmao.gsfc.nasa.gov/pubs/office_notes.

Putman, W. M., and S.-J. Lin, 2007: Finite-volume transport on various cubed-sphere grids. *J. Computat. Phys.*, **227**, 55–78.

Ricciardulli, L., and R. Garcia, 2000: The excitation of equatorial waves by deep convection in the NCAR Community Climate Model (CCM3). *J. Atmos. Sci.*, **57 (21)**, 3461–3487.

Richter, J. H., A. Solomon, and J. T. Bacmeister, 2014: On the simulation of the quasi-biennial oscillation in the Community Atmosphere Model, version 5. *J. Geophys. Res. Atmos.*, **119**, 3045–3062, doi:10.1002/2013JD021122.

Rienecker, M. M., and Coauthors, 2011: MERRA: NASA's Modern-Era Retrospective Analysis for Research and Applications. *J. Climate*, **24**, 3624–3648, doi:10.1175/JCLI-D-11-00015.1.

Scaife, A. A., N. Butchart, C. D. Warner, D. Stainforth, W. Norton, and J. Austin, 2000: Realistic quasi-biennial oscillations in a simulation of the global climate. *Geophys. Res. Lett.*, **27 (1)**, 3481–3484, doi:10.1029/2000GL011625.

Scaife, A. A., and Coauthors, 2014: Predictability of the quasi-biennial oscillation and its northern winter teleconnection on seasonal to decadal timescales. *Geophys. Res. Lett.*, **41**, 1752–1758, doi:10.1002/2013GL059160.

528 Schirber, S., E. Manzini, T. Krismer, and M. Giorgetta, 2014a: The quasi-biennial oscillation in
529 a warmer climate: sensitivity to different gravity wave parameterizations. *Climate Dyn.*, **45**,
530 825–836, doi:10.1007/s00382-014-2314-2.

531 Schirber, S., E. Manzini, and M. J. Alexander, 2014b: A convection-based gravity wave param-
532 eterization in a general circulation model: Implementation and improvements on the QBO. *J.*
533 *Adv. Model. Earth Sys.*, **6**, 264–279, doi:10.1002/2013MS000286.

534 Schoeberl, M. R., A. R. Douglass, R. S. Stolarski, S. Pawson, S. E. Strahan, and W. Read, 2008:
535 Comparison of lower stratospheric tropical mean vertical velocities. *J. Geophys. Res.*, **113**,
536 D24109, doi:10.1029/2008JD010221.

537 Seviour, W. J. M., N. Butchart, and S. C. Hardiman, 2012: The Brewer-Dobson circulation inferred
538 from ERA-Interim. *Quart. J. Roy. Meteor. Soc.*, **138**, 878–888, doi:10.1002/qj.966.

539 Solomon, S., J. T. Kiehl, R. R. Garcia, and W. L. Grose, 1986: Tracer transport by the diabatic
540 circulation deduced from satellite observations. *J. Atmos. Sci.*, **43 (15)**, 1603–1617.

541 Stephan, C., and M. J. Alexander, 2015: Realistic simulations of atmospheric gravity waves over
542 the continental U.S. using precipitation radar data. *J. Adv. Model. Earth Sys.*, **7**, 823?835, doi:
543 10.1002/2014MS000396.

544 Takahashi, M., 1996: Simulation of the stratospheric quasi-biennial oscillation using a general
545 circulation model. *Geophys. Res. Lett.*, **23 (6)**, 661–664, doi:10.1029/95GL03413.

546 Taylor, K., R. J. Stouffer, and G. A. Meehl, 2012: An overview of CMIP5 and the experiment
547 design. *Bull. Amer. Meteor. Soc.*, **93**, 485–498, doi:10.1175/BAMS-D-11-00094.1.

548 Thompson, D. W. J., M. P. Baldwin, and J. M. Wallace, 2002: Stratospheric connection to Northern
549 Hemisphere wintertime weather: Implications for prediction. *J. Climate*, **15**, 1421–1428.

Watanabe, S., Y. Kawatani, Y. Tomikawa, K. Miyazaki, M. Takahashi, and K. Sato, 2008: General aspects of a T213L256 middle atmosphere general circulation model. *J. Geophys. Res.*, **113**, D12110, doi:10.1029/2008JD010026.

Wheeler, M., and G. Kiladis, 1999: Convectively coupled equatorial waves: Analysis of clouds and temperature in the wavenumber-frequency domain. *J. Atmos. Sci.*, **56**, 374–399, doi:10.1175/1520-0469(1999)056⟨0374:CCEWAO⟩2.0.CO;2.

Yao, W., and C. Jablonowski, 2015: Idealized quasi-biennial oscillations in an ensemble of dry GCM dynamical cores. *J. Atmos. Sci.*, **72**, 2201–2226.

LIST OF FIGURES

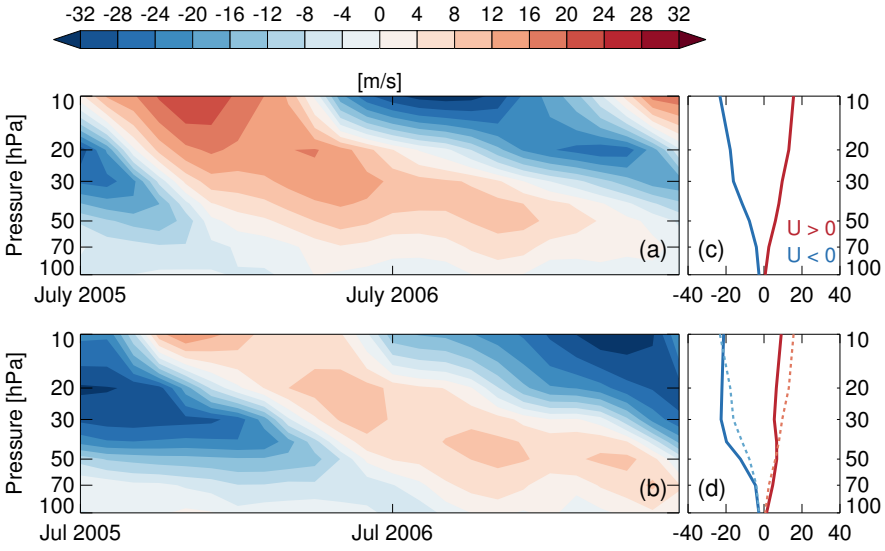

603 FIG. 1. Monthly-averaged zonal mean zonal wind as a function of pressure and time averaged between 10°S
604 and 10°N for (a) NR and (b) MERRA-2. Panels c and d show the average eastward (red) and westward (blue)
605 winds. The lines from panel c are overplotted on panel d as the dashed lines for ease of comparison.

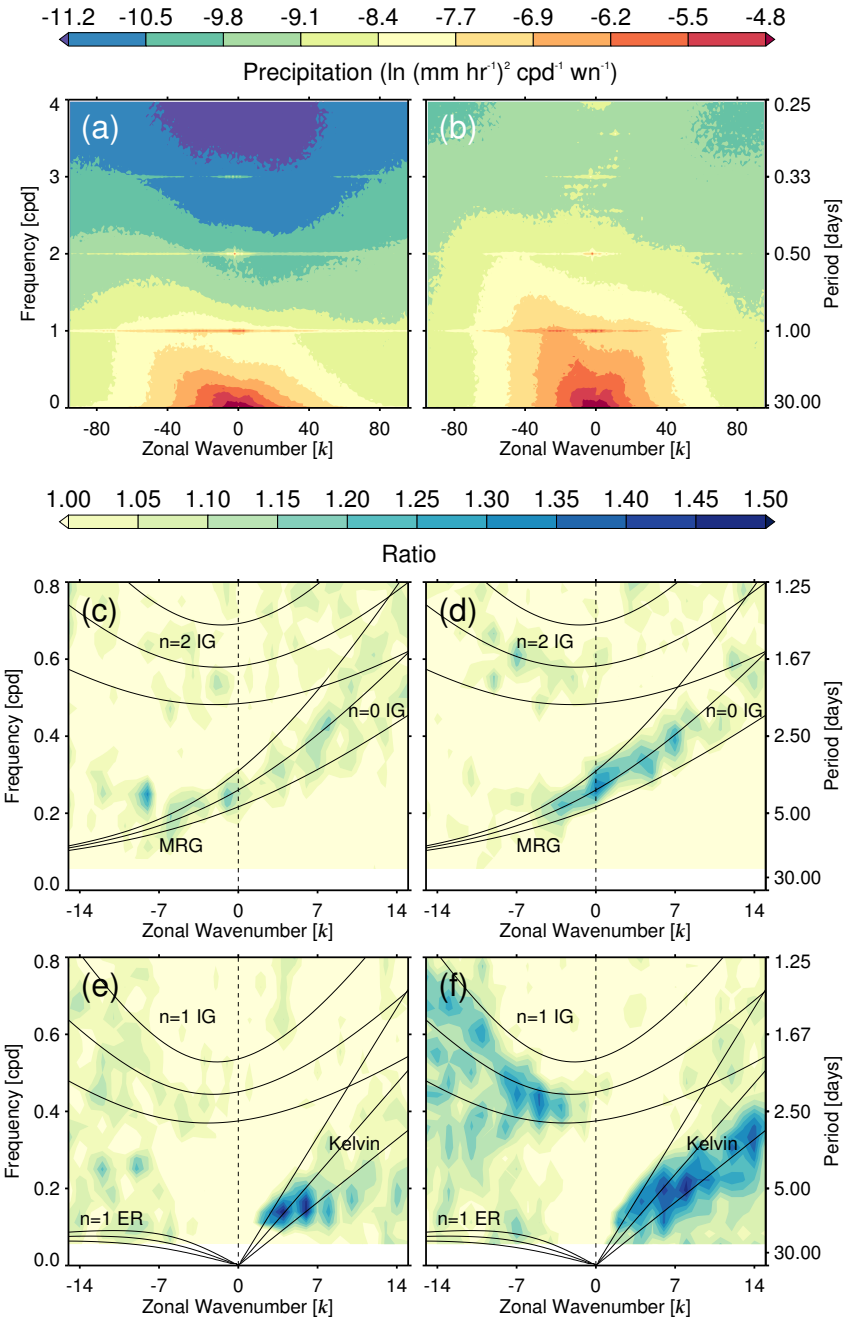

606 FIG. 2. Averaged wavenumber-frequency precipitation spectra for (a) NR and (b) TRMM between 15°S and
607 15°N, NR (c) antisymmetric and (e) symmetric components of precipitation variance, and TRMM (d) antisym-
608 metric and (f) symmetric components of normalized precipitation variance (as in Wheeler and Kiladis (1999)).
609 Theoretical dispersion curves for even and odd meridional mode number equatorial waves for equivalent depths
610 of 12, 25, and 50 m are also plotted, assuming a zero wind basic state.

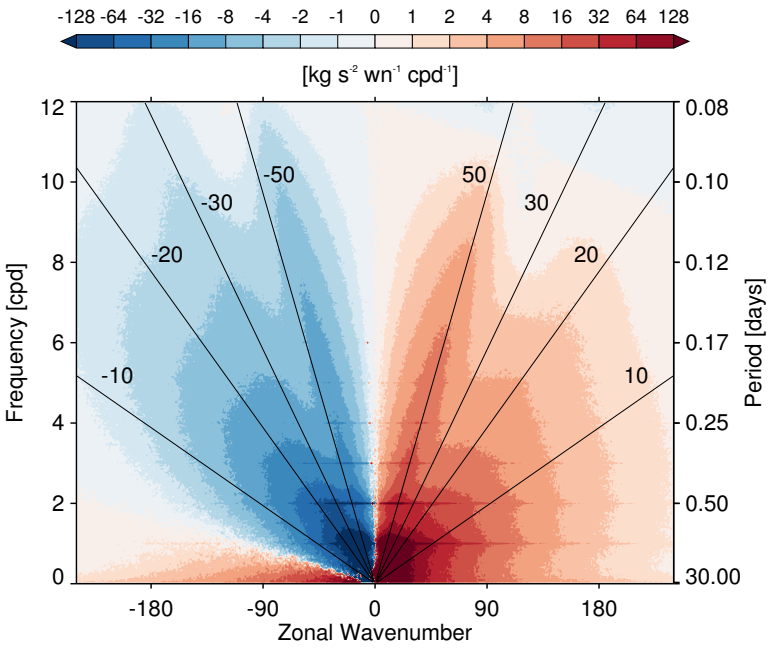

611 FIG. 3. NR zonal wavenumber-frequency spectrum of vertical EP-flux averaged between 10°S and 10°N and
612 ∼118–100 hPa. Eastward propagating waves are displayed with positive flux and westward waves with negative
613 flux. Black lines are phase speeds relative to the ground in m s^{-1}.

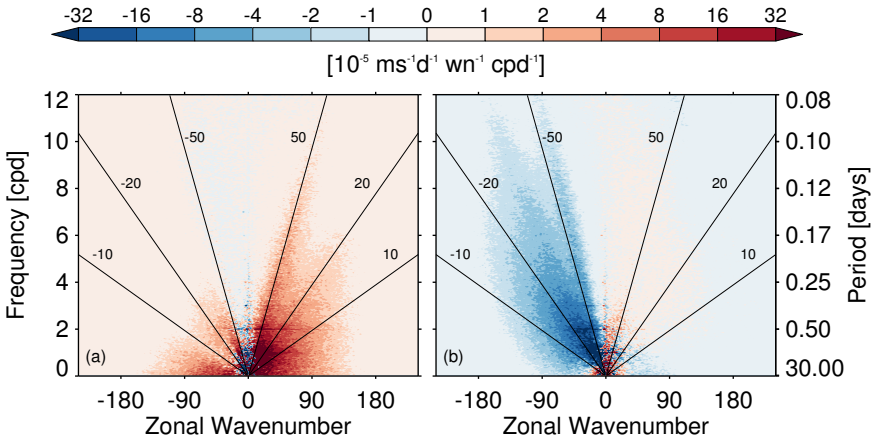

FIG. 4. NR zonal wavenumber-frequency spectra of EP-flux divergence averaged between 10°S and 10°N and ∼20–10 hPa for (a) August 2005 and (b) July 2006. Black lines are phase speeds relative to the ground in m s^{-1}.

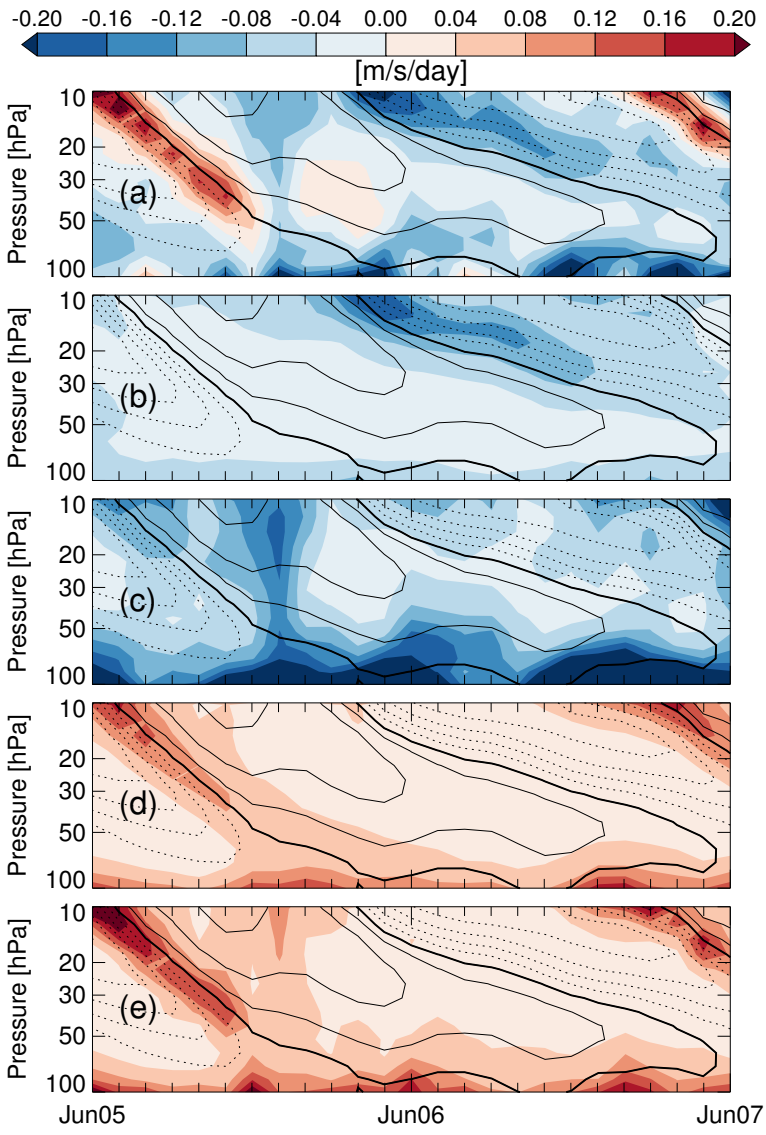

FIG. 5. (a) NR total EP-flux divergence versus pressure and time, (b) negative small-scale contribution to EP-flux divergence, (c) negative large-scale, low-frequency contribution, (d) positive small-scale contribution, and (e) positive large-scale, low-frequency contribution. Black contours are zonal mean zonal wind, where the thick solid line is 0 m s^{-1}, the contour interval is 4 m s^{-1}, and the dashed contours are negative. All panels are calculated from monthly spectra and averaged between 10°S and 10°N. Large-scale, low-frequency refers to waves with $1 \leq |k| \leq 11$ ($\lambda_x \approx 3600$ km) and $\omega < 1.0$ cpd. Small-scale refers to waves with $|k| \geq 12$.

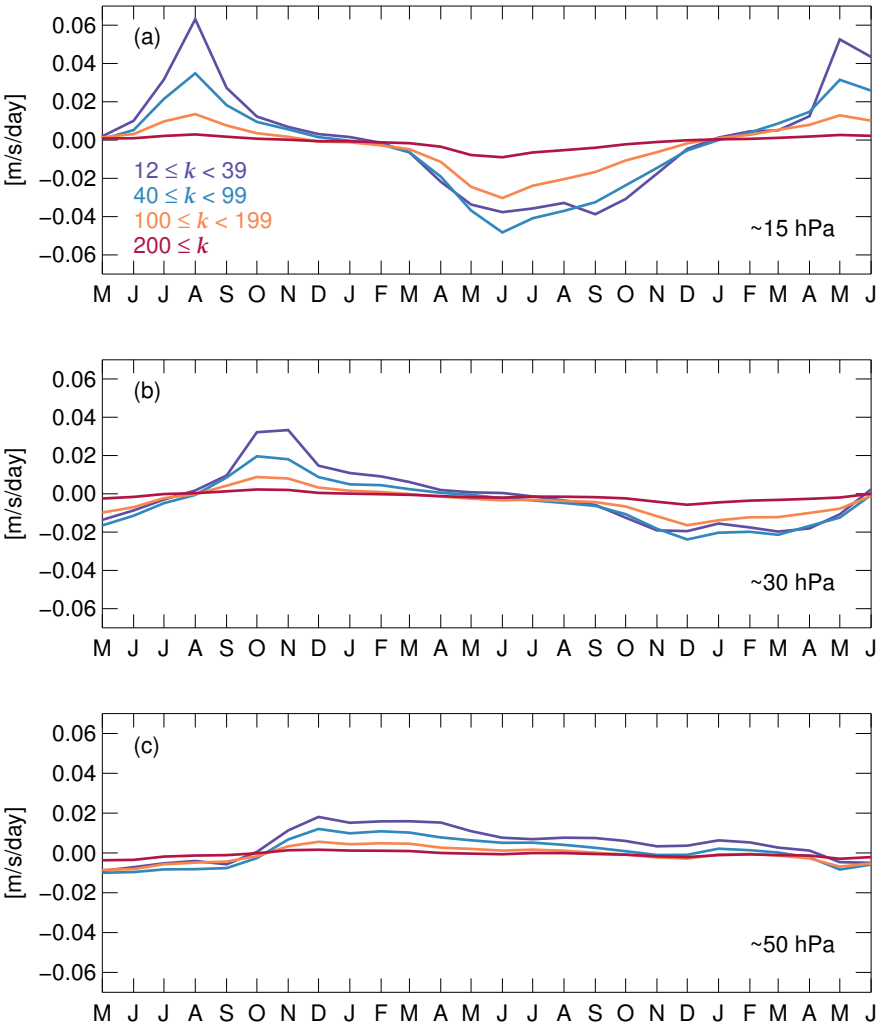

623 FIG. 6. NR EP-flux divergence versus time at (a) ∼15 hPa, (b) ∼30 hPa, and (c) ∼50 hPa for small-scale
624 waves in different zonal wavenumber bins averaged between 10°S and 10°N.

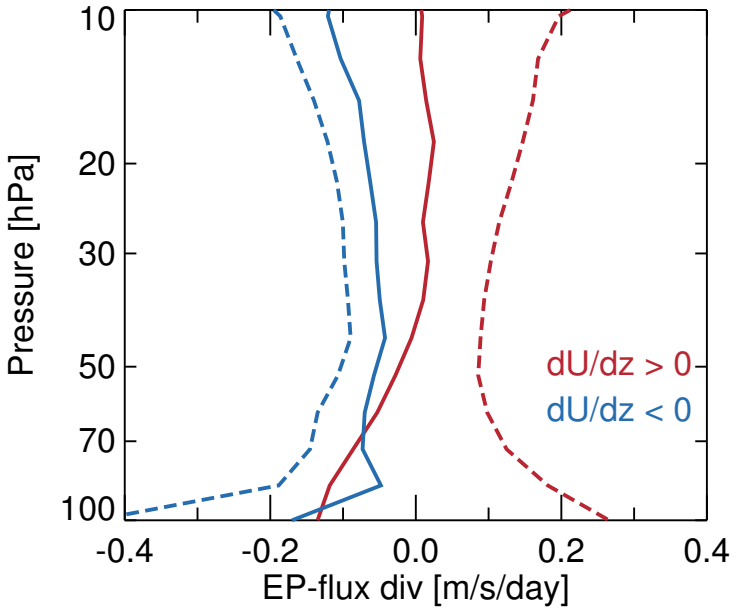

625 FIG. 7. NR EP-flux divergence as a function of pressure from both eastward and westward waves averaged
626 over eastward shear zones (solid red line) and westward shear zones (solid blue line) compared to only eastward
627 waves in eastward shear zones (dashed red line) and only westward waves in westward shear zones (dashed blue
628 line). The averages are from July 2005–June 2007 and between 10°S and 10°N.

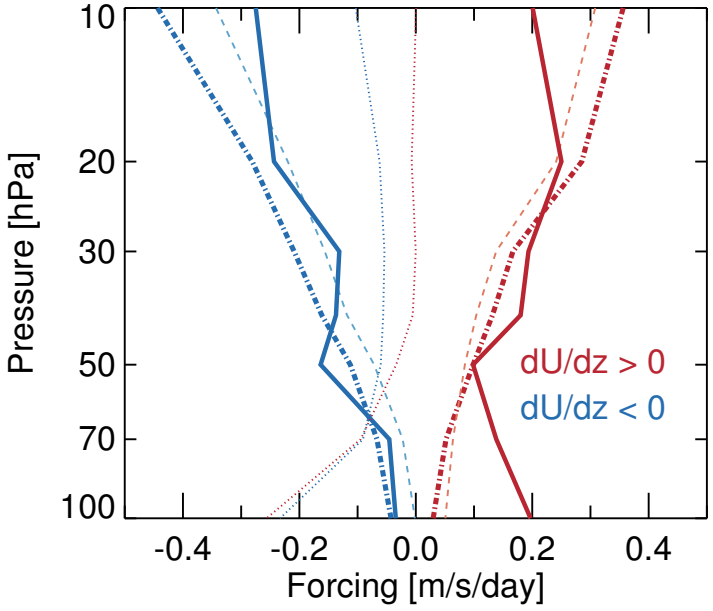

FIG. 8. The sum (thick dotted-dashed lines) of the resolved EP-flux divergence (thin dotted lines) and parameterized GWD (thin dashed lines) averaged between 10°S and 10°N as a function of pressure in NR compared to the total zonal force (LHS of Eq. 1) in MERRA-2 (thick solid lines) averaged over eastward (red) and westward (blue) shear phases of the QBO from July 2005–June 2007.

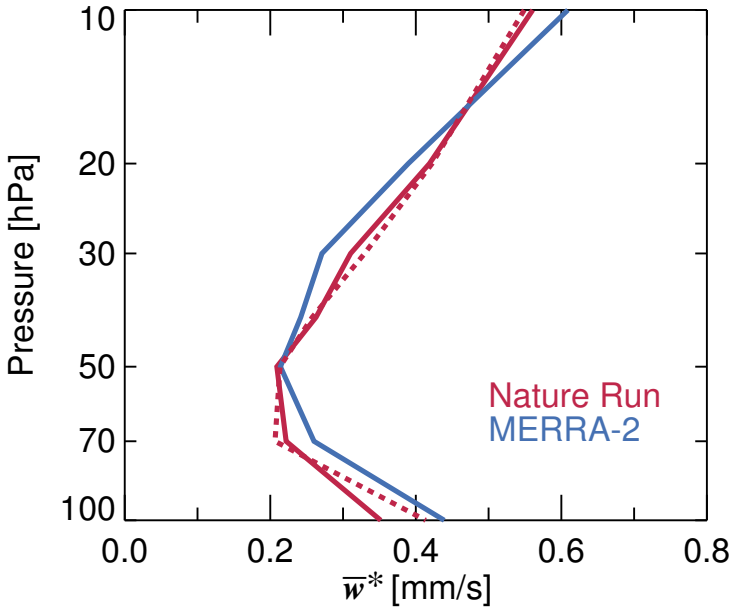

633 FIG. 9. NR (red) and MERRA-2 (blue) $\overline{w}^*$ averaged between 10°S and 10°N as a function of pressure, aver-
634 aged over July 2005–June 2007. The solid red line shows $\overline{w}^*$ calculated by iteratively solving the thermodynamic
635 equation, as described in the text. The dashed red line shows $\overline{w}^*$ calculated with the kinematic method referenced
636 in the text.

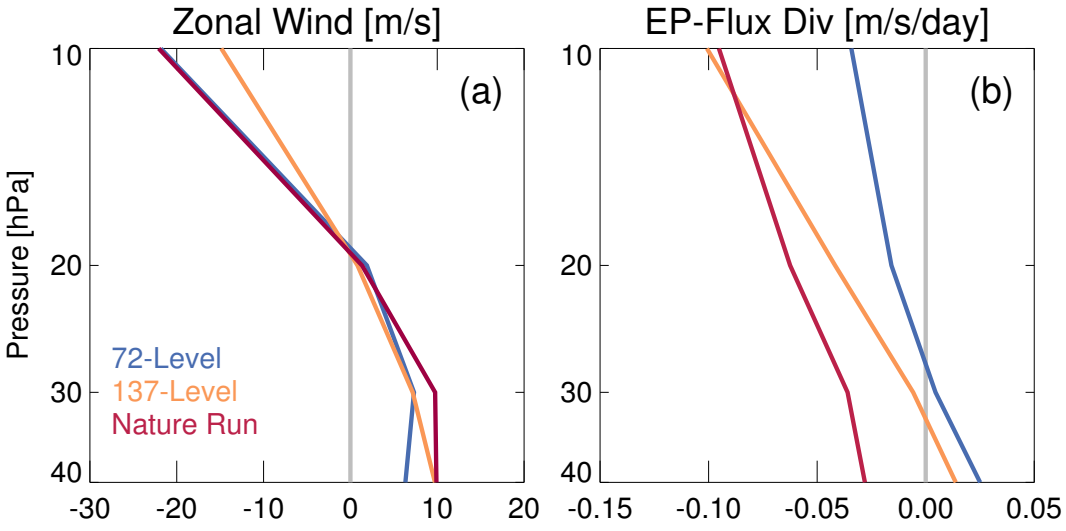

FIG. 10. (a) Zonal mean zonal wind and (b) EP-flux divergence as a function of pressure for a run with 1° horizontal resolution and 72 vertical levels (blue), a run with 1° horizontal resolution and 137 vertical levels (orange), and (red) the NR (0.0625° horizontal resolution and 72 vertical levels) averaged over the descending westward phase of the QBO between 10°S and 10°N.